

ARTICLE

# Hydrodynamic Performance of Open-frame Deep Sea Remotely Operated Vehicles Based on Computational Fluid Dynamics Method

Qianrong Li<sup>1</sup> Baoji Zhang<sup>2\*</sup>

1. Merchant Marine College, Shanghai Maritime University, Shanghai, 201306, China

2. College of Ocean Science and Engineering, Shanghai Maritime University, Shanghai, 201306, China

---

ARTICLE INFO

*Article history*

Received: 19 November 2021

Accepted: 3 December 2021

Published Online: 12 January 2022

---

*Keywords:*

ROV

CFD

Resistance performance

Motion stability

Numerical simulation

---

ABSTRACT

The resistance performance and motion stability of deep sea remotely operated vehicles (ROVs) subjected to underwater motion conditions are studied on the basis of the unsteady Reynolds-averaged Navier-Stokes method combined with the six-degree-of-freedom equation of motion to quickly and accurately predict them. In the modeling process, we consider the complexity of ROV geometry and thus reduce the model to a series of regular geometries to maximize the position and weight of the original components. The grid and value slots of an ROV are divided, and the surface is reconstructed. The forward, backward, transverse, floating, and submerged resistance of ROVs are simulated and compared with existing experimental forces to determine the accuracy of the calculation method. Then, the oblique navigation of the ROV on the horizontal and vertical planes is studied. Furthermore, the motion response of the ROV to direct horizontal motion, heave, pitch, and yaw are studied. The force, moment, and motion time curves are obtained. The stability of ROV motion is analyzed to provide technical support for the safety of ROVs.

## 1. Introduction

Remotely operated vehicles (ROVs) are unmanned underwater vehicles with acoustic and optical sense systems. An umbilical cable is used in ROVs to provide energy and transmit signals by remote control. It can accomplish high-intensity and high-load work under complex sea conditions and can be used in many fields, such as oceanographic survey, pipeline inspection, and offshore structural maintenance. In the development of

ROVs and in actual operations, their safety and stability are important considerations, and their resistance characteristics are the premise and basis of ROV motion stability. Therefore, the resistance characteristics of ROVs should be accurately predicted to build a foundation for ROV motion control. At present, the methods for accurately obtaining the hydrodynamic performance of ROVs subjected to underwater motion include the captive mode test method and computational fluid dynamics

---

\*Corresponding Author:

Baoji Zhang,

College of Ocean Science and Engineering, Shanghai Maritime University, Shanghai, 201306, China;

Email: [zbj1979@163.com](mailto:zbj1979@163.com)

DOI: <https://doi.org/10.30564/jms.v4i1.4115>

Copyright © 2022 by the author(s). Published by Bilingual Publishing Co. This is an open access article under the Creative Commons Attribution-NonCommercial 4.0 International (CC BY-NC 4.0) License. (<https://creativecommons.org/licenses/by-nc/4.0/>).

(CFD) numerical simulation method. The captive mode test method mainly includes the linear resistance test, spiral arm test, circular motion test, and plane motion mechanism (PMM) test, which is currently the most widely used in testing hydrodynamic performance. Zhang et al. (2010)<sup>[1]</sup> took an open-frame ROV as the research object and obtained the hydrodynamic coefficient with the captive mode test method. Juan et al. (2011)<sup>[2]</sup> used PMM technology to perform a concussion test on a full-scale open-frame ROV and compared the test results with the results of the Morison equation. Fan and Lian (2012)<sup>[3]</sup> used a large-amplitude horizontal PPM to conduct an in-plane oblique navigation test on a deep-sea ROV and obtained the hydrodynamic coefficient via multiple regression.

Although the captive mode test method achieves certain accuracy, it is not conducive to the development and design of low-cost ROVs due to the long test time and high cost. With the rapid development of computer technology, CFD methods can be used to predict the hydrodynamic performance of ROVs as they have become a common method in the early design stage of ROVs. Leong et al. (2015)<sup>[4]</sup> developed a numerical model to predict the pure sway motion of an underwater vehicle at different lateral and longitudinal positions relative to a large underwater vehicle using the CFD method. Kang et al. (2005)<sup>[5]</sup> used CFD software to simulate the periodic heave motion of an underwater submersible body and compared the obtained data with the model test results. Alexander et al. (2007)<sup>[6]</sup> used CFD software to study the resistance performance of underwater robots. The calculation results are consistent with the experimental data. Zhang et al. (2010)<sup>[7]</sup> calculated the hydrodynamic coefficient for a long-endurance underwater vehicle. Wang et al. (2011)<sup>[8]</sup> took a five-degree-of-freedom disc-shaped underwater robot as the research object and used CFD software to calculate the resistance. Chin and Lau (2012)<sup>[9]</sup> used the CFD software ANSYS-CFX to calculate the hydrodynamic performance of a complex-shaped ROV system and verified the theoretical calculations through model tests. Nedelcu et al. (2018)<sup>[10]</sup> provided a model used for simulation and modeling to obtain the hydrodynamic characteristics of an ROV using ANSYS-CFX. Badawy et al. (2013)<sup>[11]</sup> calculated hydrodynamic coefficients using the CFD software ANSYS-CFX. The numerical simulation is in good agreement with the experimental data. José et al. (2015)<sup>[12]</sup> used ANSYS-CFX software to calculate the drag coefficient of an ROV. Wang et al. (2014)<sup>[13]</sup> developed a mathematical model of an underwater vehicle based on CFD calculations, strip theory, and open-water tests. Skorpa (2002)<sup>[14]</sup> simplified

an open-frame ROV and used different turbulence models to study the wake distribution of the ROV during underwater motion. Vaz et al. (2010)<sup>[15]</sup> compared two viscous solvers for the accurate prediction of the maneuvering forces of streamlined submersibles using CFD calculations and so on. Yu et al. (2018)<sup>[16]</sup> calculated the hydrodynamic performance of a six-degree-of-freedom (6DOF) ROV under different working conditions on the basis of the CFD method. Chin et al. (2018)<sup>[17]</sup> used STAR CCM<sup>+</sup>™ and WAMIT™ to compute the hydrodynamic damping coefficients and added mass coefficients of an ROV. Andra et al. (2018)<sup>[18]</sup> conducted a CFD analysis for an ROV in a horizontal plane for different velocities to obtain the hydrodynamic force characteristics. Tadeusz et al. (2018)<sup>[19]</sup> used CFD to calculate the pressure of the propeller of an ROV and thereby optimize its propulsion. Juan et al. (2016)<sup>[20]</sup> used a viscous flow solver to accurately predict the maneuverability coefficient of an ROV. Christian et al. (2013)<sup>[21]</sup> analyzed the hydrodynamic behavior of an ROV under different flow conditions. The results of the model show good agreement with those in published research. Hung et al. (2013)<sup>[22]</sup> presented a numerical simulation of a recently developed ROV utilizing theoretical and experimental work to obtain the vehicle's hydrodynamic coefficients and a Laboratory Virtual Instrument Engineering Workbench (LabVIEW) based numerical model to predict its behavior. Lau et al. (2008)<sup>[23]</sup> proposed a new experimental method to determine the added mass and drag coefficients of an ROV on the basis of the classical free decay test; the experiment results agreed with those of the CFD program. Muljowidodo et al. (2009)<sup>[24]</sup> used CFD to identify the fluid characteristics on a thruster. James et al. (2014)<sup>[25]</sup> presented a methodology to increase an ROV's capabilities by optimizing its drag profile through a combination of CFD modeling and subscale experiments. Collectively, the existing studies on the hydrodynamics performance of ROVs at home and abroad mainly focus on the calculation of the simplified open-frame ROV resistance. Studying the stability of ROVs requires the accurate prediction of their hydrodynamic performance. Therefore, the current work summarizes previous research results on the basis of a deep sea ROV model and simulates the forward, backward, transverse, floating, and submerged resistance of the ROV with the Reynolds-averaged Navier-Stokes (RANS) method. The results are compared with the experimental outcomes. The resistance of the ROV under direct horizontal navigation and that under oblique navigation are studied. Then, the motion responses of the ROV under direct horizontal motion, heave, pitch, and yaw are studied with a 6DOF equation

to obtain the corresponding force and moment curves. The stability of ROV motion is analyzed to provide technical support for the safety of ROV.

## 2. Theoretical Background

The CFD technique is used to assist in the calculation of ROV resistance. The turbulent flow field around the ROV is analyzed with the general CFD software STAR CCM<sup>+</sup>™.

### 2.1 Control Equation

The whole flow field uses the continuity equation and RANS equations as the governing equations (2017)<sup>[26]</sup>.

$$\frac{\partial U_i}{\partial x_i} = 0 \quad (1)$$

$$\rho \frac{\partial U_i}{\partial t} + \rho U_j \frac{\partial U_i}{\partial x_j} = -\frac{\partial \hat{p}}{\partial x_i} + \frac{\partial}{\partial x_j} \left( \mu \frac{\partial U_i}{\partial x_j} - \overline{\rho u_i u_j} \right) + f_i^* \quad (2)$$

where  $U_i=(U,V,W)$  is the velocity component in the  $x_i=(x, y, z)$  direction;  $\rho$ ,  $\hat{p}$ ,  $\mu$ ,  $-\overline{\rho u_i u_j}$ , and  $f_i^*$  are the fluid density, static pressure, fluid viscosity, Reynolds stresses, and body forces per unit volume, respectively.

### 2.2 Turbulence Model

The turbulence model adopts the renormalization group  $k-\hat{a}$  model, and the forms of the turbulence energy transport equation and energy dissipation transport equation are as follows (2017)<sup>[27]</sup>.

$$\rho \frac{dk}{dt} = \frac{\partial}{\partial x_j} \left[ (\alpha_k \mu_{eff}) \frac{\partial k}{\partial x_j} \right] + G_k + G_b - \rho \epsilon - Y_M \quad (3)$$

$$\rho \frac{d\epsilon}{dt} = \frac{\partial}{\partial x_j} \left[ (\alpha_\epsilon \mu_{eff}) \frac{\partial \epsilon}{\partial x_j} \right] + C_{1\epsilon} \frac{\epsilon}{k} (G_k + C_{3\epsilon} G_b) - C_{2\epsilon} \rho \frac{\epsilon^2}{k} \quad (4)$$

where  $\mu_{eff}$  is the effective dynamic viscosity; and  $k$  and  $\epsilon$  are the turbulent kinetic energy and turbulent dissipation rate, respectively.  $G_k$  is the generation of turbulent kinetic energy by the mean velocity gradients.  $G_b$  is the generation of turbulent kinetic energy by buoyancy.  $Y_M$  represents the contribution of the fluctuating dilatation to compressible turbulence.  $C_{1\epsilon}$ ,  $C_{3\epsilon}$ , and  $C_{2\epsilon}$  are empirical constants.

### 2.3 Motion Equation of ROV

While establishing the motion equation of the ROV, we establish two reference coordinate systems (Figure 1). One is a fixed coordinate system  $O_o X_o Y_o Z_o$  fixed on the earth; the other is a moving system  $OXYZ$  fixed on the ROV. The origin of the moving coordinate system is located at the center of mass of the ROV. The motion

equations can be written as (2005)<sup>[28]</sup>.

$$\frac{dB}{dt} + \Omega \times B = F \quad (5)$$

$$\frac{dK}{dt} + \Omega \times K + U \times B = M \quad (6)$$

where  $B$  is the momentum of ROV,  $\Omega$  is the angular velocity,  $F$  is the external force, and  $K$  is the moment of momentum.  $U$  is the speed of the ROV, and  $M$  is the resultant moment.

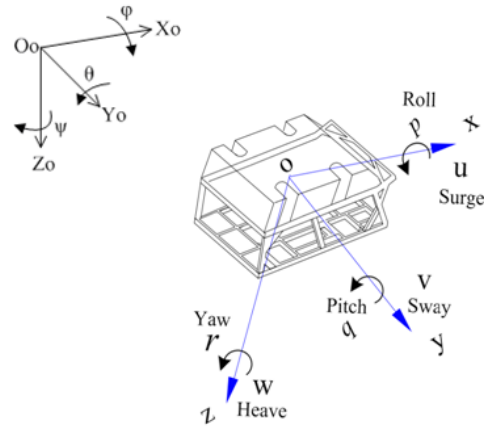


Figure 1. CAD SolidWorks model for ROV and its body-fixed coordinate system

## 3. ROV Model

The principal dimension and related parameters of the model are shown in Table 1. The scale ratio of the model is 1:1.6. The upper part of the main hull is buoyant material, the lower part of the truss is made of steel, and the other parts are simplified.

Table 1. Parameters of ROV model

| Parameter   | Unit              | Value               |
|---|-------------------|---------------------|
| Length of ROV model (L)                             | m                 | 1.88                |
| Width of ROV model (B)                              | m                 | 1.13                |
| Height of ROV model (H)                             | m                 | 1.06                |
| Mass of ROV model (M)                               | Kg                | 500                 |
| Moments of inertia relative to the x axis ( $I_x$ ) | kg.m <sup>2</sup> | 264                 |
| Moments of inertia relative to the y axis ( $I_y$ ) | kg.m <sup>2</sup> | 450                 |
| Moments of inertia relative to the z axis ( $I_z$ ) | kg.m <sup>2</sup> | 450                 |
| Center of gravity of ROV ( $x_G, y_G, z_G$ )        | M                 | (0.94, 0.185, 0.28) |

### 3.1 Computation Domain and Boundary Conditions

The computation domain and boundary conditions are roughly shown in Figure 2. Let the length of the ROV flow direction be  $L$ . The length from the inlet to the front of the body is  $3.5 L$ , the length from the rear to the

outlet of the body is 7.5 L. The height and width of the calculation domain are both 3.5 L. The inlet conditions are determined by flow velocity. The outlet conditions are given on the convection of the vertical and horizontal planes of symmetry.

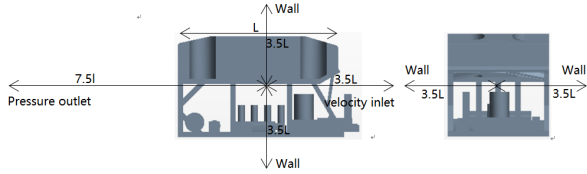


Figure 2. Computing domain and boundary conditions

### 3.2 Near Wall Modeling

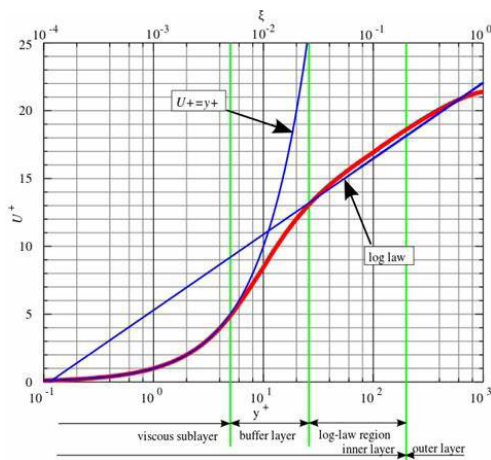


Figure 3. Law of the Wall (1995) [29]

To solve the turbulence problem in this work, we use the near wall model for the near-wall region of the ROV. The estimation of the first cell size  $y$  is based on the ITTC (International Towing Tank Conference) standard method and is given in the function of the non-dimensional wall distance  $y^+$  and the local Reynolds number  $R_e$  of the ROV.

The expression for  $y^+$  coefficient is

$$y^+ = \rho u_T \frac{y}{\mu} \quad (7)$$

where  $u_T$  is the velocity friction defined as

$$u_T = \sqrt{\tau_w / \rho} \quad (8)$$

$$y = \frac{y^+ L}{R_e \sqrt{C_f / 2}} \quad (9)$$

$$C_f = \frac{0.075}{(\log_{10} R_e - 2)^2} \quad (10)$$

where  $L$  is the length of the ROV and  $C_f$  is the friction drag coefficient of the plate.

The  $y^+$  variations of the ROV model for  $U=1.0$  m/s

are presented in Figure 4. The precision of the  $y^+$  values of the ROV determines the quality of the boundary layer solution that affects the friction force. The range of the  $y^+$  values is  $0.1 < y^+ < 40$ .

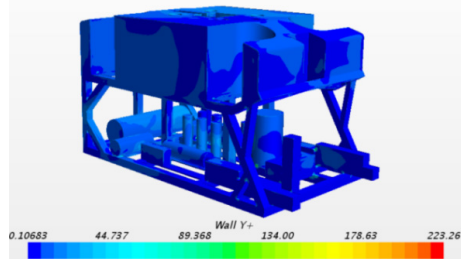


Figure 4. Wall  $y^+$  coefficient of ROV

### 3.3 Meshing

The whole calculation domain is meshed through body mesh division with right angle cutting. Given that the size of the original model is large and considering the limitation of calculation time and computer performance, we adopt a sparse grid size for the watershed and encrypt the grid only near the ROV. The final number of meshes is 5.46 million. Figures 5 and 6 indicate that the mesh near the ROV is locally refined. For calm water resistance predictions, the time step size is set to be  $0.005 * L/U$ .

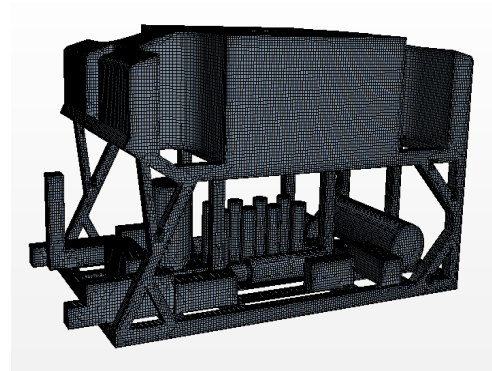


Figure 5. ROV meshing

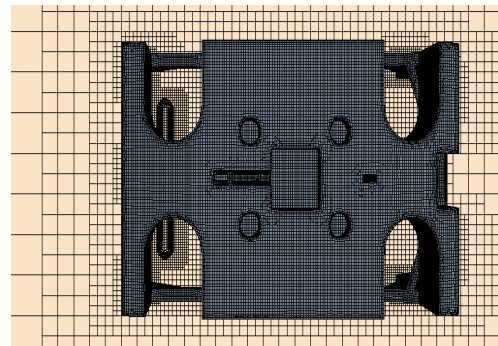


Figure 6. Grid horizontal section meshing of ROV



## 4. Convergence Analysis of CFD Calculation Results

The uncertainty of CFD simulation results determines the usefulness of data. Comparing the results obtained by different researchers using different evaluation methods is difficult. Therefore, the CFD uncertainty analysis becomes an important task in CFD research and applications (2012) [30]. This section analyzes the uncertainty of CFD according to the ITTC regulation, that is, verification and validation.

### 4.1 Verification

In this section, the cutting volume mesh is selected as a case to analyze the uncertainty of the longitudinal resistance of the ROV during direct horizontal navigation. Three grid models are established with the grid refinement ratio  $r_G=1.414$ . The free surface mesh and waveform diagram are shown in Table 2.

**Table 2.** Meshing and section pressure

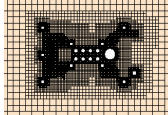
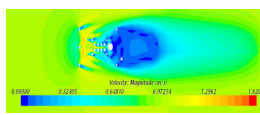
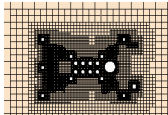
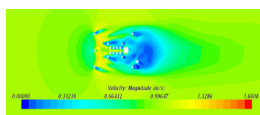
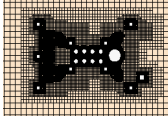
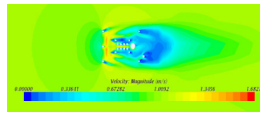
| Mesh configuration | Horizontal mesh distribution  | Section speed (m/s)   |
|--------------------|---|---|
| Coarse mesh        |  |  |
| Middle mesh        |  |  |
| Dense mesh         |  |  |

Table 2 indicates that the three grids clearly present speed cloud maps. The speed of the coarse mesh near the ROV is uneven, and the velocity cloud map obtained by the finely encrypted mesh is relatively uniform.

The error E is defined in Equation (11).

$$E(\%) = \left( \frac{D-S}{D} \right) \times 100 \quad (11)$$

The grid convergence ratio is expressed by the definition in Equation (12).

$$R_G = \frac{\varepsilon_{21}}{\varepsilon_{23}} \quad (12)$$

where  $\varepsilon_{21}=S_2-S_1$  and  $\varepsilon_{32}=S_3-S_2$ . The precision order  $P_G$ ,

correction factor  $C_G$ , and grid uncertainty  $U_G$  are defined as follows:

$$P_G = \frac{\ln(\varepsilon_{32} / \varepsilon_{21})}{\ln(r_G)} \quad (13)$$

$$C_G = \frac{r_G^{P_G} - 1}{r_G^{P_G} - 1} \quad (14)$$

$$U_G = \left| C_G \frac{\varepsilon_{21}}{(r_G^{P_G} - 1)} \right| + \left| (1 - C_G) \frac{\varepsilon_{21}}{(r_G^{P_G} - 1)} \right| \quad (15)$$

where the precision limit order ( $P_{th}$ ) in Equation (14) is 2.0, which is the formal order of CFD code precision. The longitudinal resistance coefficients calculated from the three sets of meshes are shown in Table 3. The longitudinal resistance calculation results are especially accurate when the mesh is encrypted. Table 4 shows the verification of longitudinal resistance coefficient  $C_{QT}$ , including the convergent rate  $R_G$ , order of accuracy  $P_G$ , correction factor  $C_G$ , grid spacing uncertainty  $U_G$ , error  $\sigma_{GI}^*$  with a corrected factor, corrected uncertainty value  $U_{GC}$ , and reference value for corrected numerical simulation  $S_C$ . The convergence rate  $R_G < 1$  indicates that the mesh monotonically converges. The reference value for the corrected numerical simulation  $S_C$  is 0.281, which shows that the corrected longitudinal resistance is close to the experimental value with the error of 1.08%.

**Table 3.** Longitudinal resistance coefficient of three sets of meshes ( $C_{QT} \times 10^{-3}$ )

| Scalar   | Coarse ( $S_3$ ) | Medium ( $S_2$ ) | Fine ( $S_1$ ) | Exp. (D) |
|----------|------------------|------------------|----------------|----------|
| $C_{QT}$ | 0.306            | 0.287            | 0.284          | 0.278    |
| E%D      | -10.07           | -3.24            | -2.16          | -        |

**Table 4.** Verification of calculation of total resistance coefficient

| Mesh configuration  | $R_G$ | $P_G$ | $C_G$ | $U_G$   | $\sigma_{GI}^*$ | $U_{GC}$ | $S_C$ |
|---------------------|-------|-------|-------|---------|-----------------|----------|-------|
| Cutting volume mesh | 0.157 | 5.328 | 5.336 | 0.00544 | 0.003           | 0.00244  | 0.281 |

### 4.2 Validation

Validation is the process of using experimental values to evaluate the modeling uncertainty  $U_{SM}$  of numerical simulations. If the conditions permit, then the model error  $\sigma_{SN}$  needs to be estimated. Validation determines whether verification is achieved by comparing the errors and confirming the magnitude of uncertainty. If the comparison error is less than the confirmation uncertainty, then the level of confirmation of uncertainty is achieved. The longitudinal resistance confirmation results of three

sets of meshes are shown in Table 5.  $|E|$  is less than the uncertainty  $U_V$ ; thus, the calculation results can be confirmed.

**Table 5.** Validation of results

| Error    | Results  | Confirmed uncertainty | Result  | Relationship of sizes |
|----------|----------|-----------------------|---------|-----------------------|
| $E_1$    | 0.00552  | $U_{V1}$              | 0.00775 | $ E_1  < U_{V1}$      |
| $E_{C1}$ | -0.00499 | $U_{VIC}$             | 0.00603 | $ E_{C1}  < U_{VIC}$  |

## 5. Results Analysis

### 5.1 Resistance Analysis of ROV during Direct Navigation

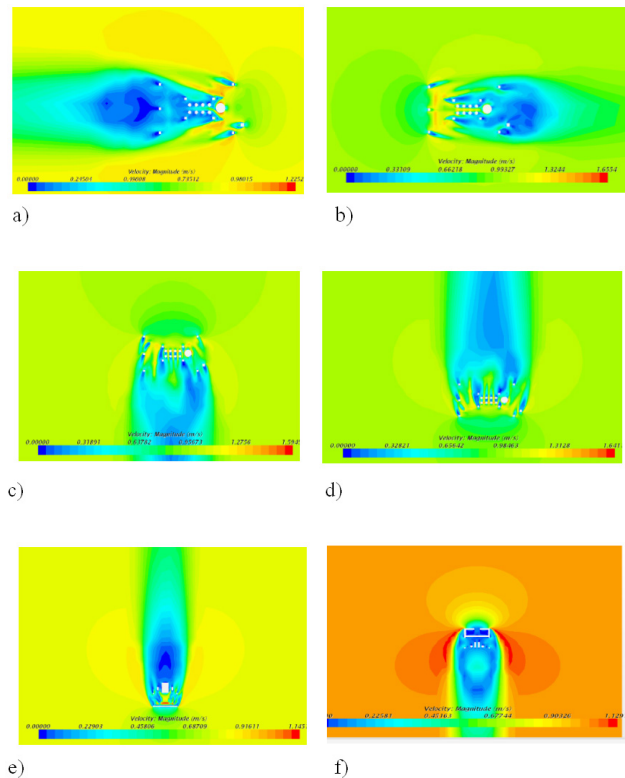
The upstream boundary is used as the velocity inlet, the downstream boundary is used as the free outlet, the surrounding boundary and model are used as walls, and simulation is performed using STAR CCM<sup>+</sup>™ software. The turbulence model is a standard  $k-\epsilon$  model. The SIMPLE(Semi-Implicit Method for Pressure Linked Equations) algorithm is used to solve the pressure-velocity coupled equations. The finite difference method is used to discretize the algebraic equations. The momentum, turbulent kinetic energy, and turbulent dissipation rate are discretized using the first-order difference scheme. The calculation speed is 0.2-1.0 m/s.

The resistance of the forward, backward, left shift, right shift, down shift, and up shift motions of the ROV at different speeds is simulated, and the numerical calculation results are compared with the test results (Fan, 2013). Table 6 shows that the simulation results are close to the experimental results and that the simulation results have high reliability and practical reference value. Through the above calculation and analysis, we find that the CFD method can well simulate the resistance of the ROV to underwater motion.

**Table 6.** Comparison of calculated and experimental forces of ROV

| Motion description | Velocity m/s         | 0.2  | 0.4   | 0.6   | 0.8   | 1.0   |
|--------------------|----------------------|------|-------|-------|-------|-------|
| Forward            | Experiment forces/N  | -    | -     | 176   | 315   | 491   |
|                    | Calculation forces/N | 37.2 | 114.4 | 189.4 | 328   | 502.4 |
|                    | Error/%              | -    | -     | 1.79  | 3.96  | 2.26  |
| Backward           | Experiment forces/N  | 41   | 119   | 171   | 304   | 475   |
|                    | Calculation forces/N | 42.4 | 120.8 | 177.8 | 315.4 | 492.7 |
|                    | Error/%              | 3.31 | 1.49  | 3.98  | 3.75  | 3.73  |

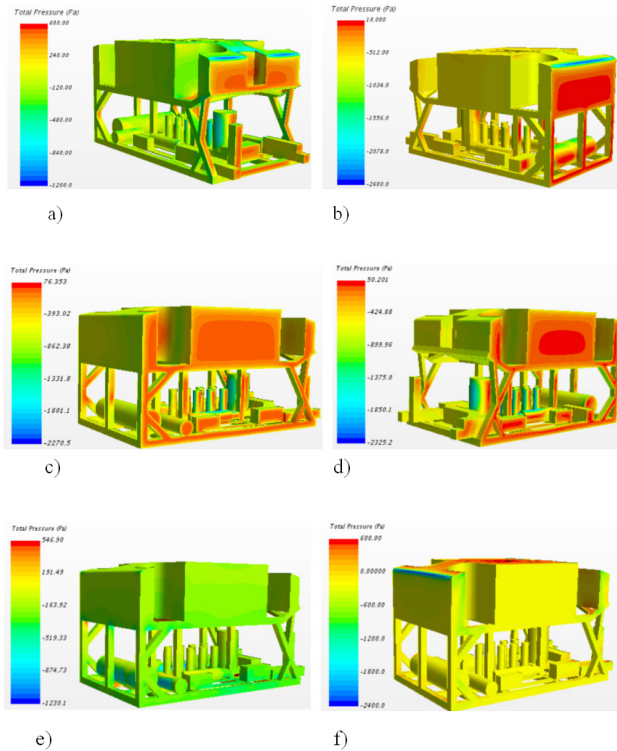
| Motion description | Velocity m/s         | 0.2   | 0.4   | 0.6   | 0.8   | 1.0    |
|--------------------|----------------------|-------|-------|-------|-------|--------|
| Left               | Experiment forces/N  | 45    | 175   | 381   | 702   | 1119   |
|                    | Calculation forces/N | 42.3  | 170.3 | 383.1 | 680.1 | 1062.8 |
|                    | Error/%              | -6.0  | -2.69 | 0.55  | -3.12 | -5.02  |
| Right              | Experiment forces/N  | 43    | 168   | 383   | 703   | 1103   |
|                    | Calculation forces/N | 42.8  | 171.9 | 387.2 | 686.0 | 1075.3 |
|                    | Error/%              | -0.47 | 2.32  | 1.10  | -2.41 | -2.51  |
| Down               | Experiment forces/N  | 46    | 181   | 400   | 713   | 1136   |
|                    | Calculation forces/N | 48.2  | 192.6 | 433.9 | 780.1 | 1213.1 |
|                    | Error/%              | 4.78  | 6.41  | 8.48  | 9.41  | 6.79   |
| Up                 | Experiment forces/N  | 41    | 186   | 401   | 696   | -      |
|                    | Calculation forces/N | 43.5  | 191.3 | 411.6 | 699.3 | 1042   |
|                    | Error/%              | 5.72  | 2.77  | 2.57  | 0.46  | -      |



**Figure 7.** Velocity contours of the ROV different views at a velocity of 1.0 m/s a). the forward view b). the backward view c). the right view d). the left view e). the down view f). the up view

Figure 7 presents the velocity contours of the design velocity of 1.0 m/s and different directions of motion.

A large low-speed zone is formed at the downstream of the ROV, which is also the main generating zone of the vortex. Therefore, a large sticking resistance is generated during the advancement process. In addition to the ROV's own frame, a large part of this low-speed area comes from the ROV. Each small part forms a low-speed area behind it. All components are densely distributed and have a large impact on the flow field. In terms of drag reduction, the water flow should pass through the interior of the ROV as smoothly as possible.



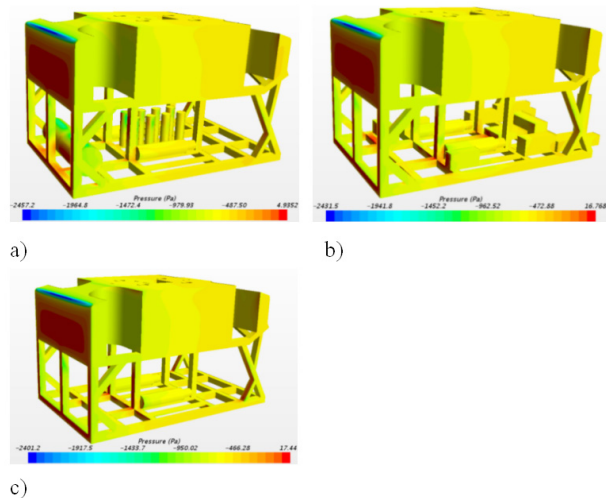
**Figure 8.** Total pressure contours of the ROV different views at a velocity of 1.0 m/s a). the forward view b). the backward view c). the right view d). the left view e). the down view f). the up view

Figure 8 shows a graph of the ROV's total pressure distribution with different motion patterns at a speed of 1.0 m/s. As a result of the upstream movement of the ROV, the front surface of the ROV is subjected to a large total fluid pressure (red color in the figure), and the total pressures in other areas are small and evenly distributed. The ROV's movement resistance is mainly related to its incident flow area and speed. When the velocity is constant in the incident flow area, the greater the ROV is, the greater the resistance will be.

### 5.2 Simplified Model Analysis

The actual ROV structure is considerably complicated and is thus not conducive to the numerical simulation

of CFD. Therefore, several small components can be simplified into regular geometries without changing the actual flow state inside the ROV. We simplify two main types of geometric components, namely, a cuboid and a cylinder. The effects of the different shape geometries inside the ROV on the resistance performance are studied separately. The original model of the ROV is simplified in three ways. As shown in Figure 9, Case 1 removes all the cuboid members in the ROV and retains all cylindrical members. Case 2 removes all the cylindrical members in the ROV and retains all the cuboid members. Case 3 removes all the cuboids and cylindrical members.



**Figure 9.** Three Simplified models schemes a). Case 1 b). Case 2 c). Case 3

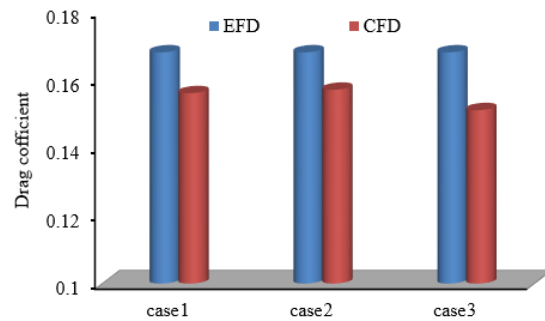


**Figure 10.** Calculation results of three schemes

Figure 10 presents a comparison of the calculated results of the three simplified models with the experimental values. The navigational resistance calculated by the three simplified schemes is smaller than that of the original model of the ROV. However, the difference between the calculation results and the data of the parent type of the three schemes is not considerably large, especially when all the components of the ROV are removed. Therefore, a simplified model can be used in the

resistance analysis to reduce the computation time.

### 5.3 Resistance Analysis of Models with Different Lengths and Heights

The principal scale of the ROV affects its resistance performance. In this work, the influence of the change of the principal scale on the resistance of the ROV is studied by changing the length (width and height are unchanged) and height (length and width are unchanged) of the ROV. The empirical formulas for calculating the ROV's navigation resistance varying with the principal scale are fitted. Table 7 shows the variation parameters of the ROV's principal scale. Table 7 presents the model obtained by reducing and enlarging Case 3 in Figure 9 in the longitudinal direction (width and height are unchanged) and height (length and width are unchanged) of the ROV. We analyze its resistance during horizontal navigation. As presented in Table 7, the navigational resistance gradually decreases with the increase of length and the decrease of height.

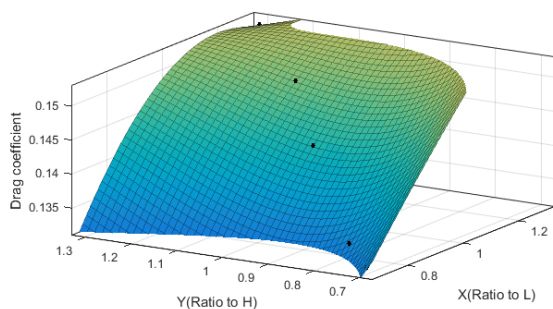
**Table 7.** Changes of the length, breadth, and height of the ROV

| L                | 0.7L  | 0.8L  | 0.9L  | 1.0L  | 1.1L  | 1.2L  | 1.3L  |
|------------------|-------|-------|-------|-------|-------|-------|-------|
| Drag coefficient | 0.207 | 0.172 | 0.155 | 0.142 | 0.129 | 0.119 | 0.118 |
| B                | 0.7B  | 0.8B  | 0.9B  | 1.0B  | 1.1B  | 1.2B  | B1.3  |
| Drag coefficient | 0.119 | 0.127 | 0.138 | 0.142 | 0.154 | 0.165 | 0.171 |
| H                | 0.7H  | 0.8H  | 0.9H  | 1.0H  | 1.1H  | 1.2H  | 1.3H  |
| Drag coefficient | 0.132 | 0.133 | 0.134 | 0.142 | 0.149 | 0.151 | 0.152 |

The empirical formula for calculating the ROV drag coefficient fitted by MATLAB software based on Table 7 is shown in Equation (16). Figure 11 presents the formula fitting diagram.

According to this formula, any type of ROV is suitable for estimating the hydrodynamic performance at the preliminary design stage as long as the principal dimensions (length, width, and height) can be a preliminary estimate of the ROV's motion resistance.

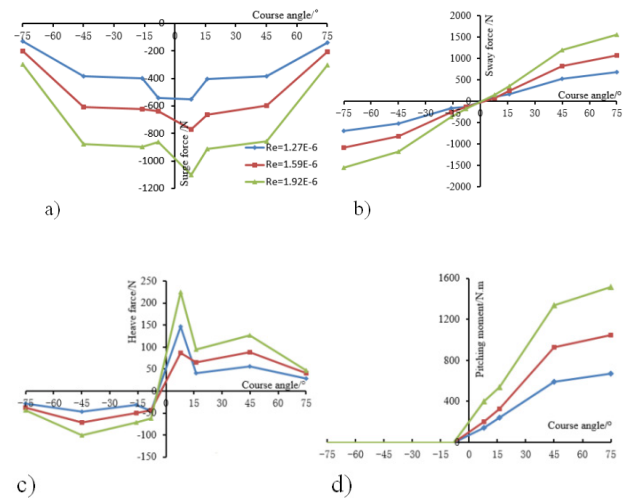
$$C_d = 0.04939 - 0.102 \sin(-0.3137\pi XY) + 0.1608 \exp(-(1.752 Y)^2) \quad (16)$$



**Figure 11.** Formula Fitting Diagram

### 5.4 Resistance Analysis of ROV's Oblique Navigation on the Horizontal Plane

The Re values are  $1.27E^{-6}$ ,  $1.59E^{-6}$ , and  $1.72E^{-6}$ . The course angles are  $-8^\circ$ ,  $+8^\circ$ ,  $-16^\circ$ ,  $+16^\circ$ ,  $-45^\circ$ ,  $+45^\circ$ ,  $-75^\circ$ , and  $+75^\circ$ . The force and moment of the ROV's oblique navigation on the horizontal plane are calculated by the CFD software star-ccm+. Figures 12 a), b), c), and d) respectively present the surge force, sway force, heave force, and pitching moment of the ROV's oblique navigation on the horizontal plane. As shown in Figure 12a), when the ROV level is tilted, the surge force increases as the speed increases. At the same speed, the smaller the drift angle is, the greater the longitudinal resistance will be. When the drift angle is between  $+15^\circ$  and  $+45^\circ$  or between  $-15^\circ$  and  $-45^\circ$ , the surge force does not change much, thereby indicating that the transverse current has little effect on the ROV. This result is explained as follows. As the ROV is an open-frame type, the parts of its body are arranged irregularly. Therefore, when a large drift angle occurs, the area behind the flow does not change much. When the drift angle exceeds  $45^\circ$ , the surge force sharply decreases. As the surge force is decomposed to the transverse direction when the drift angle becomes large, the sway force becomes large.



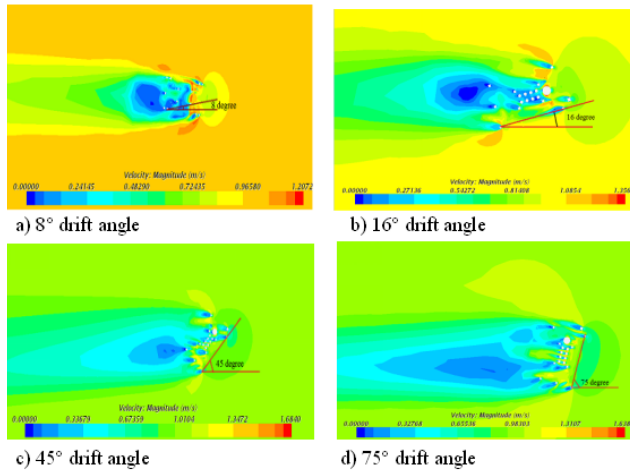
**Figure 12.** Forces and moment of the ROV's oblique navigation on the horizontal plane under different Reynolds numbers a). surge force b). sway force c). heave force d). pitching moment

Figure 12b) shows that the sway force of the ROV oblique navigation on the horizontal plane is relatively large and that the sway force increases with speed. At the same speed, the sway force increases as the drift angle increases. When the drift angle increases, the surge resistance is reduced. Thus, special attention should be paid to the influence of transverse currents on the main



heading when the ROV is performing underwater oblique navigation.

Figures 12c)-12d) indicate that the heave force of the ROV's oblique navigation on the horizontal plane is small and that the heave force increases with speed. At the same speed, the heave force decreases as the drift angle increases. The downward pitching moment increases with speed. At the same speed, it increases as the drift angle increases, and the upward pitching moment is considerably small.



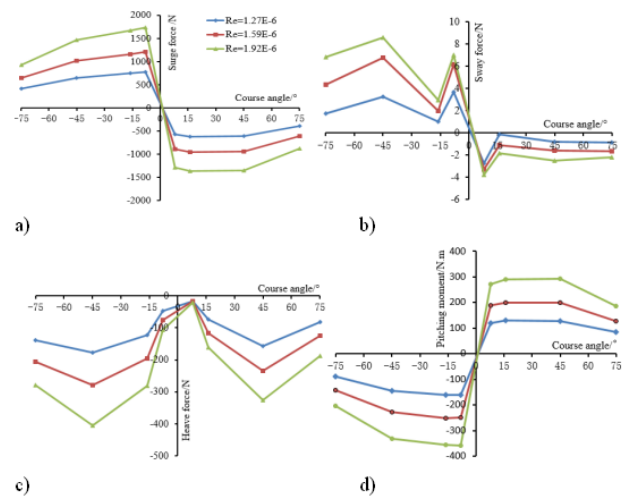
**Figure 13.** Velocity contours at different drift angles of ROV's oblique navigation on the horizontal plane

Figure 13 shows the velocity contours of a 0.5 m section at different drift angles of the ROV's oblique navigation on the horizontal plane. As the drift angle increases, the low-pressure region of the ROV attachment also becomes large. The presence of the low-pressure region affects the motion stability and equipment performance of the ROV, especially for deep water operations.

### 5.5 Resistance Analysis of ROV's Oblique Navigation on the Vertical Plane

The Re values are  $1.27E^{-6}$ ,  $1.59E^{-6}$ , and  $1.72E^{-6}$ . The course angles are  $-8^\circ$ ,  $+8^\circ$ ,  $-16^\circ$ ,  $+16^\circ$ ,  $-45^\circ$ ,  $+45^\circ$ ,  $-75^\circ$ , and  $+75^\circ$ . The force of the ROV is calculated with the CFD software star-ccm+. As a result of the asymmetry of the upper and lower structures of the ROV, the oblique navigation on the vertical plane calculates the drift angle from negative (water flow from above) to positive (water flow enters from the bottom). Figures 14 a), b), c), and d) are the surge force, sway force, heave force, and pitching moment of the ROV's oblique navigation on the vertical plane, respectively. As the speed increases, the surge force becomes significantly large. At the same speed, the surge

force, the sway force, and the heave force (the upward and downward flow areas of the ROV are different) all increase as the drift angle increases. The sway force and the heave force increase as the speed increases. The pitching moment increases as the speed and as drift angle increase at the same speed. The numerical simulation of the ROV's oblique navigation on the vertical plane can provide an operational basis for cleaning operations.



**Figure 14.** Forces and moment of ROV's oblique navigation on the vertical plane under different Reynolds numbers a). surge force b). sway force c). heave force d). pitching moment

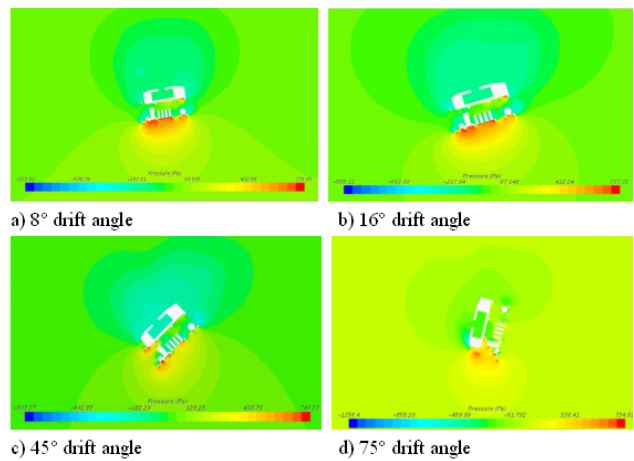


**Figure 15.** Velocity contours at different drift angles of the ROV's oblique navigation on the vertical plane

Figure 15 shows the velocity contours of the 0.5 m section at different drift angles of the ROV's oblique navigation on the vertical plane. As the drift angle increases, the upward movement speed of the ROV gradually becomes small. Therefore, the change of the drift angle affects the speed and direction of the ROV's movement, especially during deep water operations.

## 6. Movement Analysis

From the dimensional analysis and by using the Buckingham  $\pi$  theorem, we define the drag coefficient in Equation (17).

$$C_D = \frac{F}{0.5\rho S U^2} \quad (17)$$

where  $C_D$  is the drag coefficient,  $F$  is the drag force of the ROV,  $S$  is the frontal area of the ROV,  $U$  is the velocity of the ROV, and  $\rho$  is the fluid density.

Taking the ROV with horizontal motion as a case, we study the motion response of the drag coefficient in 6DOF (yaw, pitch and roll surge, sway, and heave). The drag coefficient for the ROV is a function of the Reynolds number. Thus, the similitude is satisfied by having the same Reynolds number for the two flows. The CFD study for the operating range of flow speeds (0.2 m/s ~ 1.2 m/s) shows that the drag coefficients are nearly constant for the corresponding range of Reynolds number (Figure 16).

The ROV has the largest drag in the heave direction due to its largest frontal area normal to the flow direction of about 1.49 m<sup>2</sup>. The drag force in sway is slightly larger than the drag in the surge direction due to the ROV's small frontal area. The three rotation motions, namely, yaw, pitch, and roll, are plotted against the Reynolds number in Figure 16. As observed from the plots, the ROV has the largest drag in the roll direction due to its largest mass moments of inertia. The drag force in pitch is slightly larger than the drag in the yaw direction due to the ROV's small mass moments of inertia.

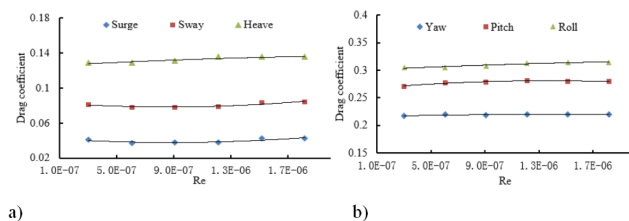


**Figure 16.** Drag coefficient versus Reynolds number. a). drag coefficient of surge, sway, heave motion b). drag coefficient of yaw, pitch, roll motion

## 7. Conclusions

The CFD method is used to study the resistance performance and motion stability of an open-frame ROV. The forward, backward, transverse, floating, and submerged resistance of the ROV are simulated and compared with existing experimental values to verify the accuracy of the calculation method. Then, the resistance performance of the ROV's oblique navigation on the

horizontal and vertical plane is studied, along with its heave, pitch, and yaw in direct horizontal navigation.

The research results show that due to the structural asymmetry of the open-frame ROV, the pitching moment, transverse force, and longitudinal force are large in the direct horizontal navigation, horizontal oblique navigation, and vertical oblique navigation, respectively. Therefore, the influence of transverse current on the ROV's motion stability should be noted in a specific ROV operation. The simulation results in this work can provide technical support for the resistance prediction and design of deep sea ROVs.

## Index of Abbreviations

|         |   |
|---------|---|
| ROV     | remotely operated vehicle                           |
| CFD     | computational fluid dynamics                        |
| PMM     | plane motion mechanism                              |
| 6DOF    | six-degree-of-freedom                               |
| LabVIEW | Laboratory Virtual instrument Engineering Workbench |
| RANS    | Reynolds-averaged Navier-Stokes                     |
| ITTC    | International Towing Tank Conference                |
| SIMPLE  | Semi-Implicit Method for Pressure Linked Equations  |

## References

- [1] Zhang, Y., Xu, G.H., Xu, X.L., et al., 2010. Mensuration of the Hydrodynamic Coefficients of the Micro Miniature Open-shelf Underwater Vehicle. *Shipbuilding of China*. 51(1), 63-72.
- [2] Juan, P., Julca, A., Julio, C.A., 2011. Experimental Evaluation of the Hydrodynamic Coefficient of a ROV Through Morison's Equation. *Ocean Engineering*. 38(17-18), 2162-2170.
- [3] Fan, S.B., Lian, L., 2012. Oblique Towing Test and Maneuver Simulation at Low Speed and Large Drift Angle for Deep Sea Open-Framed Remotely Operated Vehicle. *Journal of Hydrodynamics*. 24(2), 280-286.
- [4] Leong, Z., Ranmuthugala, D., Forrest, A., et al., 2015. Numerical investigation of the hydrodynamic interaction between two underwater bodies in relative motion. *Appl Ocean Res*. 51, 14-24.
- [5] Kang, T., Hu, K., Hu, Z.Q., et al., 2005. Research on maneuverability simulation calculation of underwater vehicle by CFX and USAERO. *Robot*. 27(6), 535-538.
- [6] Alexander, P., Maaten, F., Stephen, R.T., 18-21 June 2007. The use of computational fluid dynamics to assess the hull resistance of concept autonomous underwater vehicles. In: *Proceedings of the oceans 2007—Europe, Aberdeen, New York: IEEE*. pp.

- 1292-1297.
- [7] Zhang, H., Xu, Y.R., Cai, H.P., 2010. Using CFD software to calculate hydrodynamic coefficient. *Journal of Marine Science and Application*. 9(2), 149-155.
- [8] Wang, T., Ye, X.F., Wang, L., et al., 7-10 August 2011. Hydrodynamic analysis and optimization for dish shaped underwater robot. In: *Proceedings of the 2011 international conference on mechanics and automation*, Beijing, China. New York: IEEE. pp.1406-1411.
- [9] Chin, C., Lau, M., 2012. Modeling and testing of hydrodynamic damping model for a complex-shaped remotely-operated vehicle for control. *J Mar Sci Appl*. 11(2), 150-163.
- [10] Nedelcu, A., Trbu, O., Clinici, C., Ichimoaiei, G., 2018. CFD approach used for modelling hydrodynamic analysis and motion characteristics of a remotely operated vehicle. *IOP C Ser Earth Env*. 170, 012029.
- [11] Badawy, A.M., Omer, A.A., 2013. Dynamic analysis of remotely operated underwater vehicle model. *International Journal of Engineering Science Invention*. 2(7), 5-16.
- [12] José, B.M., Lucas, A.B., 2015. Drag evaluation of a remotely operated vehicle. *23rd ABCM International Congress of Mechanical Engineering*, December 6-11, Rio de Janeiro, RJ, Brazil.
- [13] Wang, C., Zhang, F., Schaefer, D., 2014. Dynamic modeling of an autonomous underwater vehicle. *J Mar Sci Technol*. 20(2), 199-212.
- [14] Skorpa, S., 2002. Numerical simulation of flow around remotely operated vehicle (ROV). Master's Thesis, Norwegian University of Science and Technology, Trondheim.
- [15] Vaz, G., Toxopeus, S., Holmes, S., 6-11 June 2010. Calculation of manoeuvring forces on submarines using two viscous-flow solvers. In: *Proceedings of the ASME 2010 29th international conference on ocean, offshore and arctic engineering* (Paper no. OMAE2010-20373), Shanghai, China. New York: American Society of Mechanical Engineers. pp. 621-633.
- [16] Yu, G., Wang, Z., Ling, H., 2018. Research on hydrodynamic performance of rotatable cable underwater robot. *Int J Eng Appl Sci*. 5(10), 36-42.
- [17] Chin, C.S., Lin, W.P., Lin, J.Y., 2018. Experimental validation of open-frame ROV model for virtual reality simulation and control. *J Mar Sci Technol*. 23(2), 267-287.
- [18] Andra, T.N., Catalin, F., Mihail, L.D., 2018. CFD analysis for a remotely operated vehicle in horizontal plan. *Mechanical Testing and Diagnosis*. 1, 5-10.
- [19] Teague, J., Michael Allen, J., Tom, B., 2018. The potential of low-cost ROV for use in deep-sea mineral, ore prospecting. *Ocean Eng Monitor*. 147, 333-339.
- [20] Juan, A., Ram'irez-Mac'ias, Persijn, B., et al., 2016. Hydrodynamic modeling for the remotely operated vehicle Visor3 using CFD. *Preprints, 10th IFAC Conference on Control Applications in Marine Systems* September 13-16, Trondheim, Norway.
- [21] Christian, B., Jose, R., Carlos, P.A., 2013. Hydrodynamic Assessment of a Remotely Operated Underwater Vehicle Based on Computational Fluid Dynamic-Part 1-Numerical Simulation. *CMES*. 90(2), 165-177.
- [22] Hung, D.N., Sachith, M., Dev, R., 2013. Design, modeling and simulation of a remotely operated vehicle-part1. *Journal of Computer Science and Cybernetics*. 29(4), 299-312.
- [23] Lau, W., Low, E., Seet, G., et al., 2008. Estimation of the Hydrodynamics Coefficients of an ROV using Free Decay Pendulum Motion. *Engineering Letters*. 16(3), 326-331.
- [24] Muljowidodo, K., Sapto, A.N., Nico, P., et al., 2009. Design and testing of underwater thruster for SHRIMR ROV-ITB. *Indian journal of Marine Sciences*. 38(3), 338-345.
- [25] James, J., Brian, P., 2014. Development of an adaptable monitoring package for marine renewable energy projects part II: hydrodynamic performance. *Proceedings of the 2nd Marine Energy Technology Symposium*, April 15-18, Seattle, WA.
- [26] Mingyu, K., Olgun, H., Osman, T., 2017. Numerical studies on added resistance and motions of KVLCC2 in head seas for various ship speeds. *Ocean Eng*. 140, 466-476.
- [27] Yavuz, H., Ozdemir, B.B., 2017. Numerical study of ship motions and added resistance in regular incident waves of KVLCC2 model. *Int J Nav Arch Ocean*. 9, 149-159.
- [28] Longo, J., Stern, F., 2005. Uncertainty assessment for towing tank tests with example for surface combatant DTMB model 5415. *J Ship Res*. 49(1), 55-68.
- [29] Bradshaw, P., Huang, G.P., 1995. *The Law of the Wall in Turbulent Flow*. *Proceedings: Mathematical and Physical Sciences*. Osborne Reynolds Centenary. 451(1941), 165-188.
- [30] Yang, C., Zhu, R., Miao, G., 2012. Uncertainty Analysis in CFD for Flow Simulation Around Ship Using RANS and DES. *Journal of Shang Hai Jiao Tong University*. 46(3), 430-435.